Article
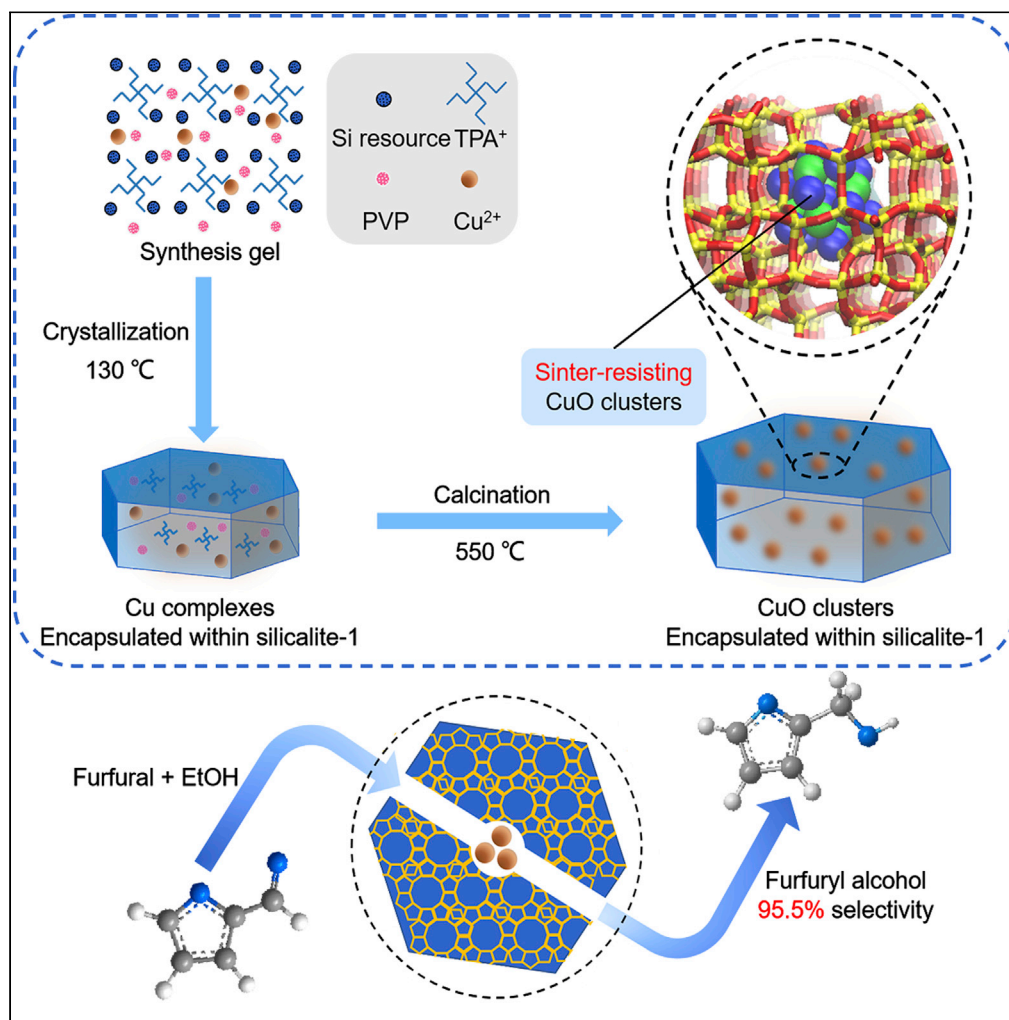
Encapsulation of CuO nanoparticles within silicalite-1 as a regenerative catalyst for transfer hydrogenation of furfural

Mingwei Weng, Zihao Zhang, Francis Okejiri, ..., Xiuyang Lu, Siyu Yao, Jie Fu

yaosiyu@zju.edu.cn (S.Y.)
jiefu@zju.edu.cn (J.F.)

Highlights

Ultrasmall CuO NPs are encapsulated in silicalite-1 matrix for CTH of furfural

Encapsulated CuO catalyst shows impressive Cu-mass-based activity of $\sim130\ hr^{-1}$

Carbon deposits can be easily removed without the obvious increase in CuO size

Strong Cu-Si interactions exist in silicalite-1-encapsulated CuO structure

Article

Encapsulation of CuO nanoparticles within silicalite-1 as a regenerative catalyst for transfer hydrogenation of furfural

Mingwei Weng,[1,2,6] Zihao Zhang,[1,6] Francis Okejiri,[3] Yue Yan,[1] Yubing Lu,[4] Jinshu Tian,[5] Xiuyang Lu,[1] Siyu Yao,[1,*] and Jie Fu[1,2,7,*]

SUMMARY

Catalytic transfer hydrogenation (CTH) of biomass-derived furfural (FAL) to fur-furyl alcohol is recognized as one of the most versatile techniques for biomass valorization. However, the irreversible sintering of metal sites under the high-temperature reaction or during the coke removal regeneration process poses a serious concern. Herein, we present a silicalite-1-confined ultrasmall CuO structure (CuO@silicalite-1) and then compared its catalytic efficiency against conventional surface-supported CuO structure (CuO/silicalite-1) toward CTF of FAL with alcohols. Characterization results revealed that CuO nanoparticles encapsulated within the silicalite-1 matrix are ~1.3 nm in size in CuO@silicalite-1, exhibiting better dispersion as compared to that in the CuO/silicalite-1. The CuO@silicalite-1, as a result, exhibited nearly 100-fold higher Cu-mass-based activity than the CuO/silicalite-1 counterpart. More importantly, the activity of the CuO@silicalite-1 catalyst can be regenerated via facile calcination to remove the surface-bound carbon deposits, unlike the CuO/silicalite-1 that suffered severe deactivation after use and cannot be effectively regenerated.

INTRODUCTION

The transformation of renewable energy resources into fuels or building block chemicals is an environmentally sustainable approach and an alternative path for fossil fuel utilization (Cha and Choi, 2015). Biomass as a renewable source of carbon is highly valued because of its ability to produce a series of value-added commodity chemicals and bio-fuels (Alonso et al., 2017; Kunkes et al., 2008). Furfural (FAL) as one of the most promising platform chemicals derived from lignocellulose-based biomass can be further upgraded to various FAL derivatives due to its highly functionalized molecular structure (Lange et al., 2012; Mariscal et al., 2016; Li et al., 2016a). Furfuryl alcohol (FOL), a well-known derivative of FAL, is commonly used as a raw material in resin production and has popularized the FAL-to-FOL selective hydrogenation process (Kijeński et al., 2002; Merlo et al., 2009; Zhang et al., 2018a, 2018b). Based on the source of the hydrogen, the FAL-to-FOL process can be broadly classified into two categories: conventional hydrogenation using molecular H_2 and transfer hydrogenation reaction consuming organic compounds as the hydrogen source (Valekar et al., 2020; Gong et al., 2017). Although Cu-based catalysts are commonly used in both hydrogenation systems, the transfer hydrogenation process with the use of methanol, ethanol, 2-propanol, or formic acid as the hydrogen donor has yielded more promising prospect (Zhang et al., 2018a, 2018b, 2020; Villaverde et al., 2015; Qiu et al., 2020; Du et al., 2018).

Cu on different support materials including C (Wang et al., 2020a, 2020b), Al_2O_3 (Zhang and Chen, 2017), SiO_2 (Du et al., 2019), ZrO_2 (Chang et al., 2016), hydroxyapatite (Putrakumar et al., 2020), etc. has been investigated as catalysts for transfer hydrogenation of FAL with some promising results. However, the susceptibility of the Cu species to sintering under the high-temperature reaction condition and during the regeneration process of the removal of the carbon deposits causes an irreversible deactivation of metal active centers (Dong et al., 2016; O'Neill et al., 2014; Lunkenbein et al., 2015). Over the years, efforts have been put toward developing sintering-resistant Cu-based catalysts featuring various strategies, including encapsulation within zeolite crystals, coating with carbon or oxide layers, strengthening the metal-support interactions, etc (Wang et al., 2019, 2020a, 2020b; Han et al., 2019; Ren et al., 2020). For instance, $Cu/CuFe_2O_4@C$ derived from the metal-organic framework and Cu@C-POP from a porous

organic polymer cavity encapsulated with Cu catalysts both displayed the enhanced catalytic performance toward FAL or 5-hydroxymethylfurfural (5-HMF) hydrogenation (Koley et al., 2020; Sarkar et al., 2021). The stabilization of metal-support surface interactions was proved in those catalysts. Although some of these strategies have exhibited signs of promising results, the developments of sintering-resistant Cu-based catalysts for efficient and low-temperature transfer hydrogenation of FAL is still a knowledge gap in the literature that requires more thorough investigation.

The present study reports a steam-assisted strategy to fabricate an ultrasmall CuO nanoparticle catalyst confined in the silicalite-1 crystal (CuO@sil-1) for transfer hydrogenation of FAL. Also, CuO nanoparticles on the surface of silicalite-1 (CuO/sil-1) were also prepared and compared to the CuO@sil-1 with respect to activity and recyclability. The structure and surface properties of the Cu-based catalysts were studied by a series of characterization techniques such as X-ray diffraction (XRD), X-ray photoelectron spectroscopy (XPS), high-resolution scanning transmission electron microscopy (STEM), X-ray absorption spectroscopy (XAS), Fourier transform infrared (FTIR), and Raman spectroscopy. Meanwhile, a reasonable model for the CuO@sil-1 catalyst was established based on the characterization results and optimized via periodic density functional theory (DFT) calculations. The superior activity and stability of the CuO@sil-1 catalyst was supported by the experimental results.

RESULTS

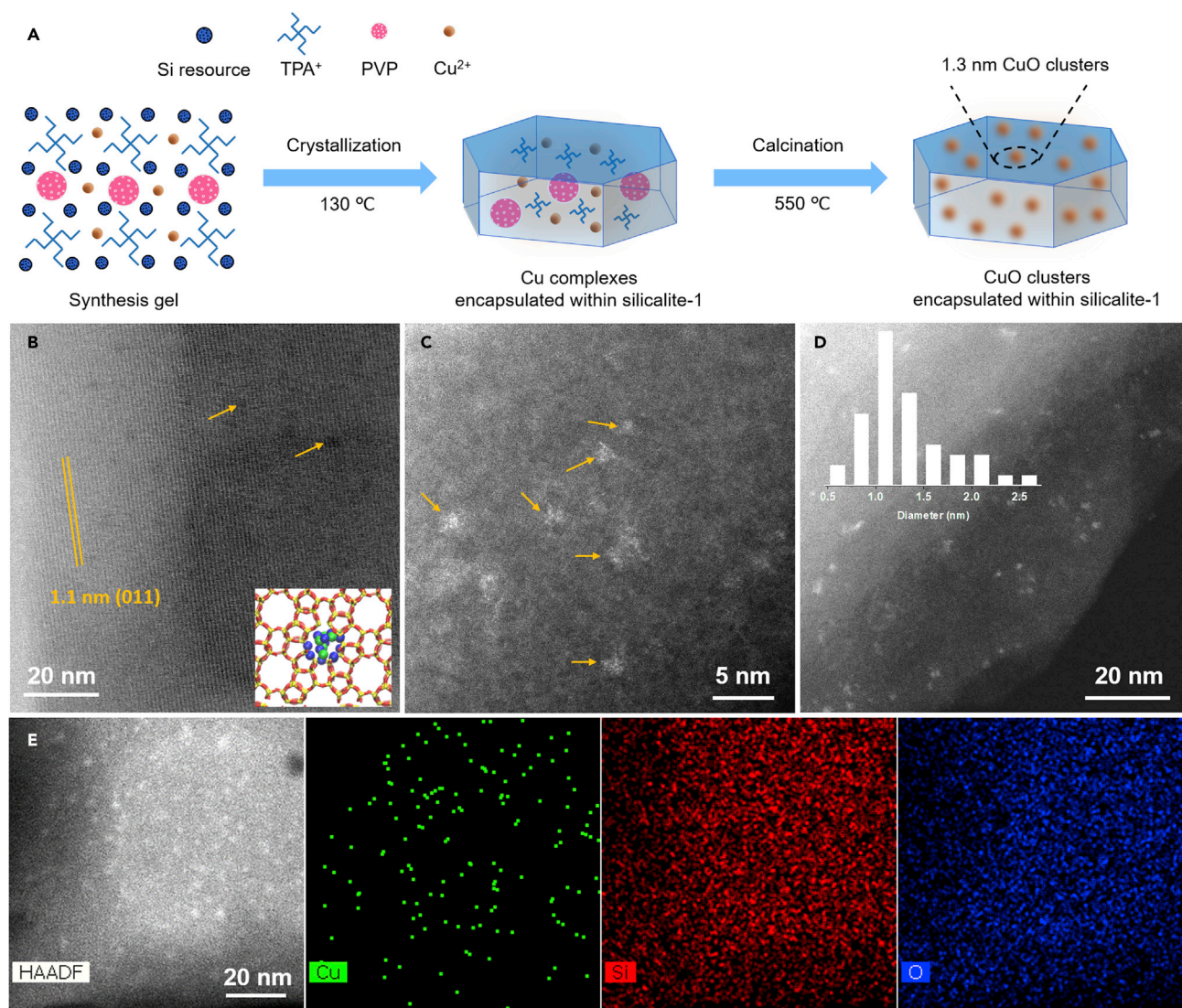### Synthesis and characterization of CuO@silicalite-1 and CuO/silicalite-1

The CuO@silicalite-1 (CuO@sil-1) was synthesized via a two-step strategy: (1) the self-assembly of Cu precursor and initial zeolitic gelation under hydrothermal process, leading to an immature sil-1-encapsulated Cu complex structure; (2) calcination in air, which transforms the Cu complex to CuO nanoparticles (NPs) within the sil-1 framework. The general synthetic process is depicted in Figure 1A. It should be noted that the excess addition of the Cu precursors prevents the crystallization of sil-1 to some extent, leading to the formation of relatively larger CuO NPs outside the sil-1 framework, namely the CuO/SiO_2 structure as seen in Figure S1. A series of Cu-based catalysts with different Cu loadings were prepared, where x refers to the actual Cu contents (Table S1) in the various catalysts as determined by inductively coupled plasma optical emission spectroscopy analyses. For instance, "3" in 3CuO@sil-1 refers to the actual Cu content in this catalyst is 3.26 wt% according to Table S1.

The XRD patterns of pristine sil-1 and 3CuO@sil-1 are shown in Figure 2A exhibits the typical MFI-type zeolite structure, which is indicative of the formation of a sil-1 crystal structure (Yan et al., 2019; Valtchev, 2002). The zeolitic five-membered ring structure can also be evidenced in the FTIR spectra in Figure 2B with the characteristic peaks located at 551 and 1230 cm^{-1}. These unique features are, however, not visible in the $7CuO/SiO_2$ and $23CuO/SiO_2$ spectra, which are indicative of a partial or complete collapse of the sil-1 structure owing to the introduction of excess Cu. Also, the (011) plane of the sil-1 structure can be indexed from the transmission electron microscopy (TEM) image in Figure 1B due to its crystallinity. The characteristic diffraction peaks are located at 2θ values of 35.5 and 38.7 for the $23CuO/SiO_2$ catalysts, and the relatively broader peaks found in $7CuO/SiO_2$ at approximately the same 2θ position indicate the formation of somewhat smaller CuO NPs in $7CuO/SiO_2$.

Figures 1B–1D show the high-resolution TEM images, in which the ultrasmall CuO clusters are identified by the yellow arrows. A representative low-resolution TEM image can be seen in Figure S2. The particle size distribution of Cu in 3CuO@sil-1 based on the TEM images in Figures 1D, S3B, and S3C is 1.3 nm on average (standard deviation: 0.49, 55 particles), which is slightly larger than the microporous size of sil-1 in Figure S4A. Fortunately, the as-synthesized sil-1 is a hierarchical porous structure that provides abundant space for the dispersion of the ultrasmall CuO clusters. The hierarchical porous nature of 3CuO@sil-1 can also be validated by the pore parameters (Table S2) and mesopore size distribution (Figure S4B). The STEM-energy dispersive spectroscopy (EDS) elemental maps of 3CuO@sil-1 in Figures 1E and S3D show a uniform distribution of Cu within the sil-1 supports with no apparent trace of large particles related to Cu species. The EDS elemental map of $23CuO/SiO_2$, although it shows a uniform distribution of CuO NPs, however, shows some relatively larger particle size CuO of approximately 7 nm, as seen in Figure S5.

Spectroscopic analysis of CuO@silicalite-1 and CuO/silicalite-1

The Raman spectra of sil-1, 3CuO@sil-1, $23CuO/SiO_2$, and commercial CuO were acquired and displayed in Figure 2C. The characteristic sil-1 band at 377 cm^{-1} is visible only in sil-1 and 3CuO@sil-1, which is

Figure 1. The synthesis and morphology characterization of 3CuO@sil-1

(A) The synthesis route for the CuO clusters encapsulated within silicalite-1 crystal.

(B–D) The representative (high-resolution) TEM images of 3CuO@sil-1 (the CuO clusters are marked by the yellow arrows), and the corresponding (D) particle size distribution in 3CuO@sil-1. (B): The bright field; (C and D): the dark field.

(E) STEM-EDS elemental mapping of 3CuO@sil-1, Cu (green), Si (red), and O (blue)

consistent with the XRD and FTIR results. Three Raman bands are observed in 23CuO/SiO$_2$ spectra at 278 (the strongest), 329, and 615 (the broadest) cm^{-1} which are consistent with the Raman features of a typical CuO (Xu et al., 1999a, 1999b). For the 3CuO@sil-1, however, new Raman bands at 293, 434, and 471 cm^{-1} are visible and quite different from those in typical CuO NPs or sil-1. It has been reported that CuO NPs with smaller sizes usually result in the Raman peak shift to the lower wavenumber (Xu et al., 1999a, 1999b); thus, we ascribed the new Raman bands found in the relative higher wavenumbers in 3CuO@sil-1 to the vibration of new Cu-O-Si or Cu-Si bonds, rather than smaller CuO NPs. The spectra of XPS indicate that the surface chemical states of Cu in both 3CuO@sil-1 and 23CuO/SiO$_2$ are predominantly Cu^{2+}, as evidenced by the two satellite peaks of Cu^{2+} in Figure 2D (Jiang et al., 2015). Meanwhile, the surface Cu in 3CuO@sil-1 seems to be slightly reduced since its Cu 2p$_{3/2}$ peak shifts to a relatively lower binding energy as compared to 23CuO/SiO$_2$. The occurrence of this charge transfer phenomenon and the new Raman features in 3CuO@sil-1 collaboratively suggest the possible existence of metal-support interaction or Cu-Si interaction.
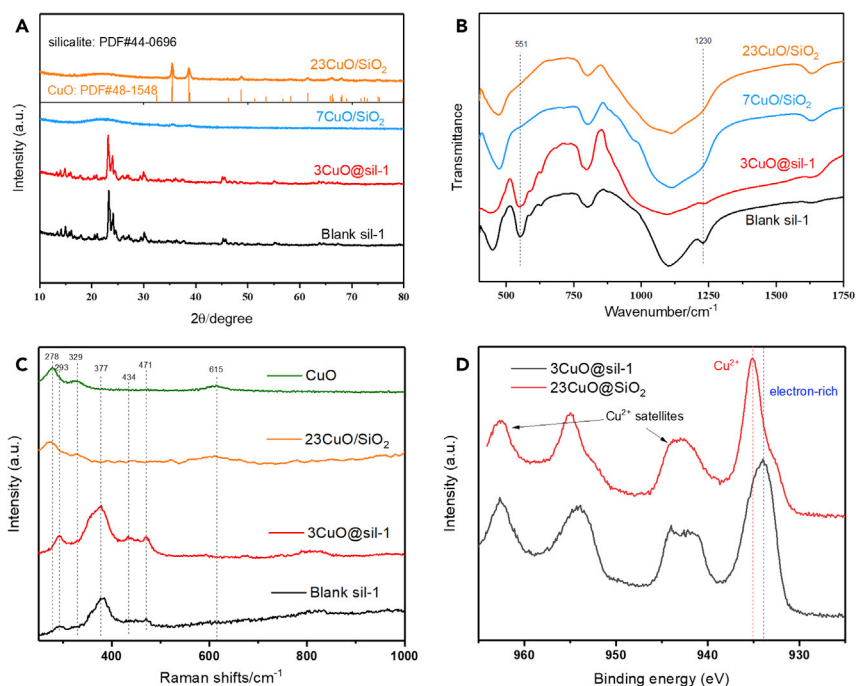
Figure 2. Spectroscopic analysis
(A and B) (A) XRD patterns and (B) FTIR spectroscopy of sil-1, 3CuO@sil-1, 7CuO/SiO₂, and 23CuO/SiO₂ catalysts.
(C) Raman spectra of blank sil-1, 3CuO@sil-1, 23CuO/SiO₂, and CuO.
(D) XPS spectra of 3CuO@sil-1 and 23CuO/SiO₂.

To further clarify the chemical states of Cu in 3CuO@sil-1 and 23CuO/SiO₂ samples, XAS was performed at the Cu K-edge. Figure 3A shows the Cu K-edge X-ray absorption near edge structure (XANES) spectra of the various catalysts alongside the reference spectra for Cu, CuO, and Cu₂O. 3CuO@sil-1 and 23CuO/SiO₂ catalysts both exhibit similar white line intensities and XANES features that are similar to CuO, indicating that the Cu species in both catalysts are predominantly Cu^{2+}, in agreement with XPS results. Figure 3B shows the Fourier transformed extended X-ray absorption fine structure (EXAFS) spectra. The two major peaks ascribed to the first and second shell coordination spheres are seen in both 3CuO@sil-1 and 23CuO/SiO₂. The first peak located at ~1.5 Å in R is typically associated with the first shell O atoms surrounding the Cu atom, (i.e., first shell Cu−O coordination). The second peak at ~2.3 Å originates from the superposition contributions from either Cu atoms (Cu−O−Cu) or Si (Cu−O−Si) atoms as these two coordinations have similar R distances (Sushkevich et al., 2020). The wavelet transform (WT) analyses of the Cu K-edge EXAFS spectra were carried out to visually identify the local coordination of Cu. The WT technique, which can differentiate the contribution of different scattering paths by decomposing the R and k signals of the EXAFS, is a powerful tool for distinguishing atoms neighboring a metal center (Funke et al., 2005; Stevens et al., 2017; Kuai et al., 2020). As seen in WT EXAFS profiles of 3CuO@sil-1 and 23CuO/SiO₂ (Figures 3C and 3D), one central maximum at $R \approx 1.2$–1.5 Å and $k \approx 4$ Å^{-1} is identified as the first shell Cu−O coordination. At a slightly higher k, a maximum at $R \approx 2$ Å and $k \approx 6$–7 Å^{-1} is proposed as the contribution of Cu−O−Si coordination that correlates with the Cu-O-Si interface. Figure 3C shows a more substantial Cu−O−Si contribution for 3CuO@sil-1 than 23CuO/SiO₂ in Figure 3D, which supports the observation of the smaller particle size and/or stronger Cu-Si interactions in 3CuO@sil-1.

Identifying catalysts' structure and electronic property by DFT calculations

To better understand the structure of 3CuO@sil-1, periodic DFT calculations (the details can be seen in the experimental section) were carried out to optimize the structure of copper-oxo species within the sil-1 crystal. The optimized structure is shown in Figures 3E and 3F. The Cu species of Cu-O-Si have a relatively lower Bader charge than that in bulk CuO cluster (−0.44 vs. 1.03 |e| in Figure S6), like the CuO nanoparticles on the surface of sil-1 (Figure S7). The valence of Cu atom in Cu-O-Si form is lower than that in Cu-O-Cu form (Figure S6). This further evidences the strong Cu-O-Si interaction or the electronic transfer from Si to Cu, which
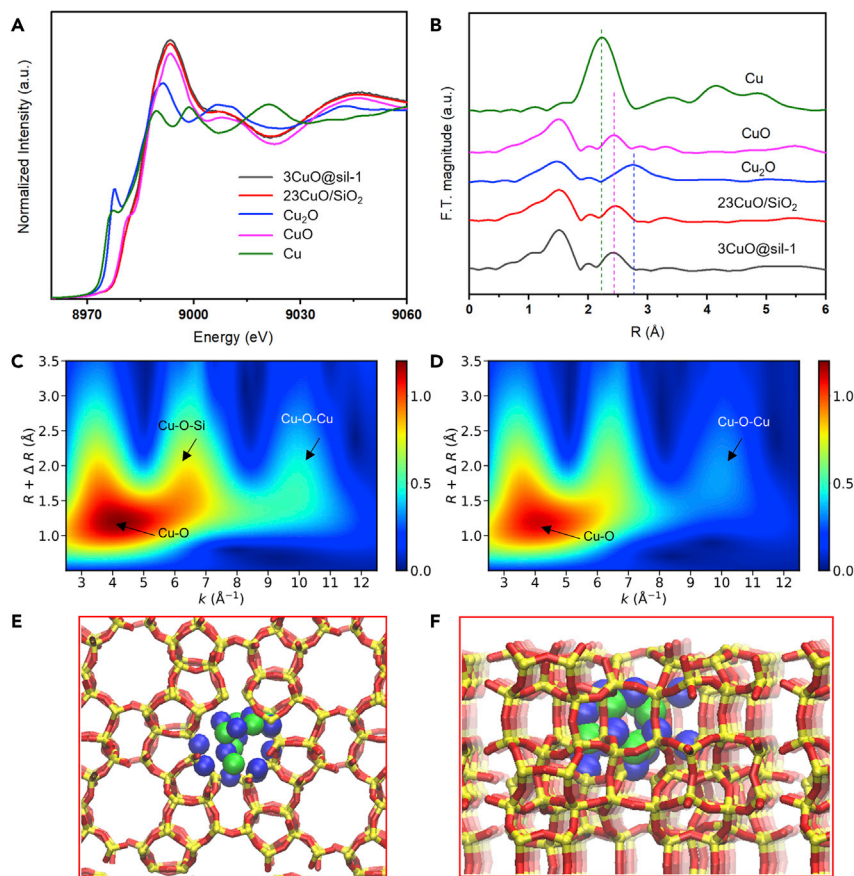
Figure 3. Structure characterization of 3CuO@sil-1 and 23CuO/SiO$_2$

(A–F) (A) Cu K-edge XANES spectra and (B) Fourier transformed EXAFS spectra of 3CuO@sil-1, 23CuO/SiO$_2$, reference Cu$_2$O, CuO, and Cu; Wavelet transform (WT) EXAFS spectra of (C) 3CuO@sil-1 and (D) 23CuO/SiO$_2$ catalysts; the optimized structure of 3CuO@sil-1 from (E) top view and (F) side view, red: O in sil-1, yellow: Si, blue: O in CuO, green: Cu

perhaps explains why Raman, XPS, and XAS features of copper-oxo species inside 3CuO@sil-1 are such different from those in 23CuO/SiO$_2$ and conventional CuO NPs.

Catalytic transfer hydrogenation of furfural with alcohols

The use of alcohols as hydrogen donors in catalytic transfer hydrogenation (CTH) has been extensively investigated in which 2-propanol has been identified as the most promising candidate (Li et al., 2016b, 2020; Panagiotopoulou et al., 2014; He et al., 2018; Ramos et al., 2020; Fan et al., 2021). Using the silicalite-1 confined ultrasmall CuO (3CuO@sil-1) as the catalyst, we also investigated the effects of different alcohols including methanol, ethanol, and 2-propanol as the hydrogen donor on the CTH of FAL. As seen in Figure 4A, methanol exhibits the lowest FOL yield of 54% at 240°C; isopropanol shows a FOL yield of ~98%, which is slightly better than that 88% yield shown by ethanol. Considering the lower cost of ethanol and the huge prospects of biomass-derived ethanols (Zabed et al., 2017), ethanol was selected as the choice hydrogen donor for CTH of various Cu-based catalysts in the present study. The re-action temperature and time were equally optimized to obtain the optimal conversion efficiency and selec-tivity to FOL, as seen in Figure S8. Thereafter, the activity of the synthesized Cu-based catalysts was compared toward CTH using the optimized reaction conditions. The results are shown in Figure 4B. The sil-1 catalyst with no Cu loading (blank) produced a very low yield of FOL, indicating low catalytic activity of sil-1 catalyst toward CTH of FAL. Among the various Cu-based catalysts under review, 3CuO@sil-1 with the lowest Cu loading displayed the highest FAL conversion (93.2%) and an 88.3% yield of FOL at a reaction temperature of 240°C for 1.5 hr. The catalytic activity was found to decrease with an increasing Cu loading, as 23CuO/SiO$_2$ gave the lowest FAL conversion (41.8%) and just 15.8% yield of FOL. Also,
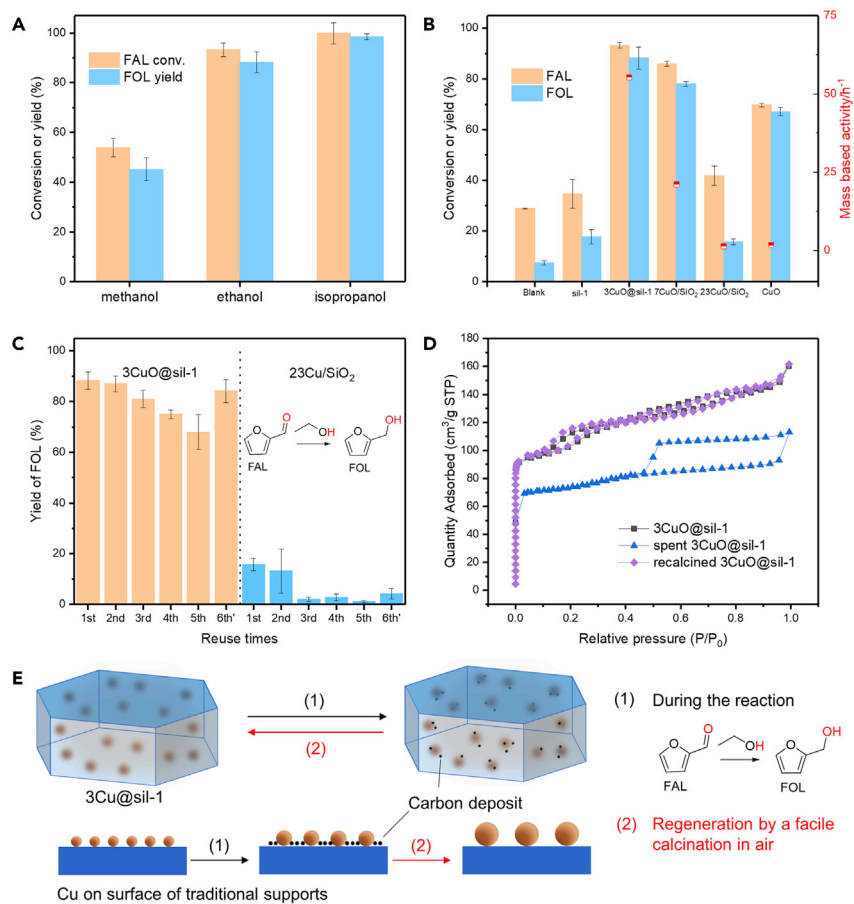
Figure 4. Catalytic activity and stability performance

(A) FAL conversion and yield of FOL over 3CuO@sil-1 with various hydrogen donors: methanol, ethanol, and isopropanol; n = 3 for each conditions.

(B) FAL conversion and yield of FOL over various catalysts; xCu representing the actual Cu loading is x wt%, n = 6 for each catalysts.

(C) Yield of FOL over fresh, reused, and regenerated 3CuO@sil-1 and 23CuO/SiO$_2$ catalysts, n = 6 for catalysts.

(D) N$_2$ adsorption-desorption isotherms of fresh, reused, and regenerated 3CuO@sil-1 catalyst.

(E) The schematic illustration of changes in different kinds of catalysts during the reaction and regeneration processes; reaction condition: 60 mg furfural, 30 mg catalyst, 6 mL hydrogen donor, 240°C, 1.5 hr.

the activity of a commercial CuO was tested toward CTH of FAL under similar reaction conditions, and it showed a 69.7% FAL conversion and 67.1% yield of FOL. Based on the actual Cu loading in Table S1, the Cu mass-based activity (MBA, mg FOL/mg Cu) of the various catalysts are calculated and displayed in Figure 4B. 3CuO@sil-1 affords nearly 100-fold higher MBA than the commercial CuO and 23CuO/SiO$_2$, which underscores the activity advantages of the encapsulated ultrasmall CuO clusters for CTH of FAL. We also compared the catalytic performance and stability of our 3CuO@sil-1 and reported Cu-based catalysts for the hydrogenation of FAL or 5-HMF, as seen in Table S3.

To clarify the optimized copper site, we also evaluated the catalytic performance of 3CuO@sil-1-H$_2$ (fresh 3CuO@sil-1 was reduced in H$_2$ at 400°C) and 3CuO@sil-1-H$_2$-air (reduced 3CuO@sil-1-H$_2$ was recalcined at 550°C in static air) toward the FAL hydrogenation. The results are shown in Figure S9. Fresh 3CuO@sil-1 and recalcined 3CuO@sil-1-H$_2$-air catalysts show significantly higher FAL conversion and FOL yield than the reduced 3CuO@sil-1-H$_2$ catalyst, indicating that the oxidized Cu species is more active for the CTH of FAL. In addition, we also explored the catalytic performance of the sil-1, 3CuO@sil-1, 7CuO/SiO$_2$, and 23CuO/SiO$_2$ for other FAL derivatives such as 5-HMF and 5-methylfurfural (5-MF). As seen in Figures S10A and S10B, 3CuO@sil-1 also performed best during all candidates for the production of 5-methylfur-furyl alcohol from 5-MF and 2,5-furandimethanol from 5-HMF.

The catalysts' reusability and regeneration performance

The reusability performance of 3CuO@sil-1 and 23CuO/SiO$_2$ catalysts was investigated at 240°C reaction temperature to compare their stability difference. The results are shown in Figure 4C. The reused catalysts were recycled by facile filtration and drying process. In both catalysts, the catalytic performance was found to decrease with an increasing number of cycles. The yield of FOL decreased from 88.3% to 68.0% over 3CuO@sil-1 catalyst across five usage cycles. Similarly, the yield of FOL decreased from 15.8% to 1.1% over 23CuO/SiO$_2$ catalyst across five usage cycles. It should be noted the rate of activity loss is significantly slower in 3CuO@sil-1 as compared to 23CuO/SiO$_2$ catalyst under similar recycling conditions. Since CuO particle size in 23CuO/SiO$_2$ is significantly larger than that in 3CuO@sil-1 sample, their support component is mostly amorphous SiO$_2$ different from crystallized sil-1. Therefore, we synthesized the surface-supported 3CuO/sil-1 catalyst via a post-impregnation method with the similar Cu loading (3 wt%), similar CuO size (Figure S11), and same support (sil-1) as 3CuO@sil-1 to compare their reuse performance. As seen in Figure S12, the catalytic activity and stability of encapsulated 3CuO@sil-1 catalyst are better than 3CuO/sil-1, further identifying the unique advantage of encapsulated structure. To understand the possible cause of deactivation (loss of activity) in 3CuO@sil-1, XRD and thermogravimetric analysis (TGA) of both fresh and reused catalysts were compared, as seen in Figures S13 and S14. The XRD patterns show a negligible difference between fresh and reused catalysts for 3CuO@sil-1, which indicates the absence of any significant particle growth or restructuring. The TGA result in Figure S14 and N$_2$ adsorption-desorption isotherms in Figure 4D on the other hand revealed the presence of carbon deposits in the reused catalyst which are responsible for the blockage of porous channels, thereby limiting the accessibility of the active site, hence, the decrease of activity.

Fortunately, the catalytic activity of 3CuO@sil-1 can be nearly fully recovered by a simple calcination process at 550°C to remove the carbon deposits. Upon the removal of the carbon deposit in 3CuO@sil-1 following the fifth usage cycle, the yield of FOL for the sixth usage cycle could be seen to have tremendously increased comparing to the fifth cycle, as seen in Figure 4C. The removal of carbon deposit is reflected in N$_2$ adsorption-desorption isotherms in Figure 4D. The surface areas (Table S2) of 3CuO@sil-1, reused 3CuO@sil-1, and recalcined 3CuO@sil-1 are 345.9, 230.3, and 353.5 m^2/g, respectively, clearly suggesting the formation and removal processes of the carbon deposits. Furthermore, there is no obvious collapse of sil-1 framework and sintering of CuO species evidenced by the FTIR spectroscopy (Figure S15), the TEM images, and EDS mapping results (Figure S16) of the spent 3CuO@sil-1. In contrast, the catalytic activity of 23CuO/SiO$_2$ could not be recovered after the same regeneration process. We attribute the permanent loss of activity in 23CuO/SiO$_2$ to irreversible sintering of CuO NPs during the reaction and the regeneration step, which can be proved by the obvious sharper XRD diffraction peaks in spent 23CuO/SiO$_2$ compared to the fresh 23CuO/SiO$_2$ (Figure S17). It should also be noted that the electron-rich Cu XPS feature of spent 3CuO@sil-1 becomes more obvious compared to the fresh catalyst (Figure S18), suggesting the catalyst should be partially reduced after the reaction. This might partially account for the slight decrease of catalytic activity of spent 3CuO@sil-1. These observations underscore the stability advantage of this unique encapsulated structure as a regenerative catalyst that can possibly meet the harsh industrialization conditions. Figure 4E depicts various changes that can occur with the encapsulated CuO structure during the reaction and regeneration processes, as well as in conventional CuO structure on an external support surface, in which the advantages of this encapsulated structure can be clearly identified.

DISCUSSION

In summary, ultrasmall CuO NPs with an average size of ∼1.3 nm confined within a silicalite-1 crystal were investigated as a potential catalyst for transfer hydrogenation of FAL. These encapsulated ultrasmall CuO NPs showed higher activity and stability toward catalytic transfer hydrogenation of FAL than surface-dispersed CuO counterparts. Ethanol with comparable performance to the commonly used 2-propanol was utilized as the hydrogen donor due to its lower cost and high availability. A series of characterization techniques, including XRD, TEM, FTIR, Raman, XPS, and XAS, was used to understand the structure of the encapsulated CuO NPs and the origin of their superior activity and stability. The ultrasmall feature of Cu species in CuO@sil-1 is ascribed to its unique confined geometry and strong Cu/Si interaction, which prevents the aggregation of the Cu species during the reaction and regeneration processes. As a result, the encapsulated CuO@sil-1 catalyst exhibits a higher MBA toward CTH of FAL than surface-supported Cu/SiO$_2$ and commercial CuO catalysts. We believe that this CuO@sil-1 catalyst holds great promise in the industrialization of biomass upgrading.

Limitations of the study

In this work, we encapsulated CuO nanoparticles within silicalite-1 zeolite for the CTH of FAL to FOL. An impressive catalytic activity and stability can be realized on our CuO@sil-1 catalyst. However, developing well-defined silicalite-1-encapsulated CuO nanoparticles with tunable pore sizes can be further studied in the future.

STAR★METHODS

Detailed methods are provided in the online version of this paper and include the following:

- KEY RESOURCES TABLE
- RESOURCE AVAILABILITY
  - Lead contact
  - Materials availability
  - Data and code availability
- METHOD DETAILS
  - Catalyst synthesis
  - Characterizations
  - DFT calculations
  - Catalytic performance evaluation
- QUANTIFICATION AND STATISTICAL ANALYSIS

AUTHOR CONTRIBUTIONS

J.F. and Z.Z. conceived the research idea. Z.Z., M.W., and Y.Y. performed the experiments, and analyzed the data. S.Y. did the XAS experiment. J.T. did the DFT calculations. Y.L. analyzed the data of XAS. X.L. and S.Y. discussed the results and raised the suggestions. J.F., Z.Z., M.W., and F.O. co-wrote and revised the paper.

DECLARATION OF INTERESTS

The authors declare no competing interests.

REFERENCES

Alonso, D.M., Hakim, S.H., Zhou, S., Won, W., Hosseinaei, O., Tao, J., Garcia-Negron, V., Motagamwala, A.H., Mellmer, M.A., Huang, K., et al. (2017). Increasing the revenue from lignocellulosic biomass: Maximizing feedstock utilization. Sci. Adv. 3, e1603301.

Cha, H.G., and Choi, K.-S. (2015). Combined biomass valorization and hydrogen production in a photoelectrochemical cell. Nat. Chem. 7, 328–333.

Chang, X., Liu, A.F., Cai, B., Luo, J.Y., Pan, H., and Huang, Y.B. (2016). Catalytic transfer hydrogenation of furfural to 2-methylfuran and

2-methyltetrahydrofuran over bimetallic copper–palladium catalysts. ChemSusChem 9, 3330–3337.

Dong, F., Ding, G., Zheng, H., Xiang, X., Chen, L., Zhu, Y., and Li, Y. (2016). Highly dispersed Cu nanoparticles as an efficient catalyst for the synthesis of the biofuel 2-methylfuran. Catal. Sci. Technol. 6, 767–779.

Du, J., Zhang, J., Sun, Y., Jia, W., Si, Z., Gao, H., Tang, X., Zeng, X., Lei, T., and Liu, S. (2018). Catalytic transfer hydrogenation of biomass-derived furfural to furfuryl alcohol over in-situ

prepared nano Cu-Pd/C catalyst using formic acid as hydrogen source. J. Catal. 368, 69–78.

Du, H., Ma, X., Yan, P., Jiang, M., Zhao, Z., and Zhang, Z.C. (2019). Catalytic furfural hydrogenation to furfuryl alcohol over Cu/SiO2 catalysts: a comparative study of the preparation methods. Fuel Process. Technol. 193, 221–231.

Fan, Y., Zhuang, C., Li, S., Wang, Y., Zou, X., Liu, X., Huang, W., and Zhu, G. (2021). Efficient single-atom Ni for catalytic transfer hydrogenation of furfural to furfuryl alcohol. J. Mater. Chem. A 9, 1110–1118.

Funke, H., Scheinost, A., and Chukalina, M. (2005). Wavelet analysis of extended x-ray absorption fine structure data. Phys. Rev. B 71, 094110.

Goedecker, S., Teter, M., and Hutter, J. (1996). Separable dual-space Gaussian pseudopotentials. Phys. Rev. B 54, 1703.

Gong, W., Chen, C., Zhang, Y., Zhou, H., Wang, H., Zhang, H., Zhang, Y., Wang, G., and Zhao, H. (2017). Efficient synthesis of furfuryl alcohol from H_2-hydrogenation/transfer hydrogenation of furfural using sulfonate group modified Cu catalyst. ACS Sustain. Chem. Eng. 5, 2172–2180.

Grossmann, A., and Morlet, J. (1984). Decomposition of hardy functions into square integrable wavelets of constant shape. SIAM J. Math. Anal. 15, 723–736.

Han, F., Yuan, M., Mine, S., Sun, H., Chen, H., Toyao, T., Matsuoka, M., Zhu, K., Zhang, J., and Wang, W. (2019). Formation of highly active superoxide sites on CuO nanoclusters encapsulated in SAPO-34 for catalytic selective ammonia oxidation. ACS Catal. 9, 10398–10408.

He, J., Li, H., Riisager, A., and Yang, S. (2018). Catalytic transfer hydrogenation of furfural to furfuryl alcohol with recyclable Al–Zr@ Fe mixed oxides. ChemCatChem 10, 430–438.

Jiang, X., Qiao, J., Lo, I.M., Wang, L., Guan, X., Lu, Z., Zhou, G., and Xu, C. (2015). Enhanced paramagnetic Cu^{2+} ions removal by coupling a weak magnetic field with zero valent iron. J. Hazard. Mater. 283, 880–887.

Kijeński, J., Winiarek, P., Paryjczak, T., Lewicki, A., and Mikołajska, A. (2002). Platinum deposited on monolayer supports in selective hydrogenation of furfural to furfuryl alcohol. Appl. Catal. A 233, 171–182.

Koley, P., Shit, S.C., Joseph, B., Pollastri, S., Sabri, Y.M., Mayes, E.L.H., Nakka, L., Tardio, J., and Mondal, J. (2020). Leveraging Cu/CuFe2O4-catalyzed biomass-derived furfural hydrodeoxygenation: a nanoscale metal-organic-framework template is the prime key. ACS Appl. Mater. Inter. 12, 21682–21700.

Kuai, C., Xu, Z., Xi, C., Hu, A., Yang, Z., Zhang, Y., Sun, C.-J., Li, L., Sokaras, D., and Dong, C. (2020). Phase segregation reversibility in mixed-metal hydroxide water oxidation catalysts. Nat. Catal. 3, 743–753.

Kunkes, E.L., Simonetti, D.A., West, R.M., Serrano-Ruiz, J.C., Gärtner, C.A., and Dumesic, J.A. (2008). Catalytic conversion of biomass to monofunctional hydrocarbons and targeted liquid-fuel classes. Science 322, 417–421.

Lange, J.P., Van Der Heide, E., van Buijtenen, J., and Price, R. (2012). Furfural—a promising platform for lignocellulosic biofuels. ChemSusChem 5, 150–166.

Li, X., Jia, P., and Wang, T. (2016a). Furfural: a promising platform compound for sustainable production of C4 and C5 chemicals. ACS Catal. 6, 7621–7640.

Li, J., Liu, J.l., Zhou, H.j., and Fu, Y. (2016b). Catalytic transfer hydrogenation of furfural to furfuryl alcohol over nitrogen-doped carbon-supported iron catalysts. ChemSusChem 9, 1339–1347.

Li, F., Jiang, S., Huang, J., Wang, Y., Lu, S., and Li, C. (2020). Catalytic transfer hydrogenation of furfural to furfuryl alcohol over a magnetic $Fe_3O_4@$ C catalyst. New J. Chem. 44, 478–486.

Lippert, G., Hutter, J., and Parrinello, M. (1999). The Gaussian and augmented-plane-wave density functional method for ab initio molecular dynamics simulations. Theor. Chem. Acc. 103, 124–140.

Lunkenbein, T., Schumann, J., Behrens, M., Schlögl, R., and Willinger, M.G. (2015). Formation of a ZnO overlayer in industrial $Cu/ZnO/Al_2O_3$ catalysts induced by strong metal–support interactions. Angew. Chem. 127, 4627–4631.

Mariscal, R., Maireles-Torres, P., Ojeda, M., Sádaba, I., and Granados, M.L. (2016). Furfural: a renewable and versatile platform molecule for the synthesis of chemicals and fuels. Energy Environ. Sci. 9, 1144–1189.

Merlo, A.B., Vetere, V., Ruggera, J.F., and Casella, M.L. (2009). Bimetallic PtSn catalyst for the selective hydrogenation of furfural to furfuryl alcohol in liquid-phase. Catal. Commun. 10, 1665–1669.

Morlet, J., Arens, G., Fourgeau, E., and Glard, D. (1982). Wave propagation and sampling theory—Part I: complex signal and scattering in multilayered media. Geophysics 47, 203–221.

O'Neill, B.J., Miller, J.T., Dietrich, P.J., Sollberger, F.G., Ribeiro, F.H., and Dumesic, J.A. (2014). Operando X-ray absorption spectroscopy studies of sintering for supported copper catalysts during liquid-phase reaction. ChemCatChem 6, 2493–2496.

Panagiotopoulou, P., Martin, N., and Vlachos, D.G. (2014). Effect of hydrogen donor on liquid phase catalytic transfer hydrogenation of furfural over a Ru/RuO2/C catalyst. J. Mol. Catal. A Chem. 392, 223–228.

Perdew, J.P., Burke, K., and Ernzerhof, M. (1996). Generalized gradient approximation made simple. Phys. Rev. Lett. 77, 3865.

Putrakumar, B., Kumar, S.P., Srinivasarao, G., Rajan, K., Rajesh, R., Rao, K.R., and Liang, T. (2020). High performance and sustainable copper-modified hydroxyapatite catalysts for catalytic transfer hydrogenation of furfural. Catalysts 10, 1045.

Qiu, M., Guo, T., Xi, R., Li, D., and Qi, X. (2020). Highly efficient catalytic transfer hydrogenation of biomass-derived furfural to furfuryl alcohol using UiO-66 without metal catalysts. Appl. Catal. A 602, 117719.

Ramos, R., Peixoto, A.F., Arias-Serrano, B.I., Soares, O.S.G., Pereira, M.F., Kubička, D., and Freire, C. (2020). Catalytic transfer hydrogenation of furfural over $Co_3O_4—Al_2O_3$ hydrotalcite-derived catalyst. ChemCatChem 12, 1467–1475.

Ren, L., Tong, L., Yi, X., Zhou, W., Wang, D., Liu, L., and Ye, J. (2020). Ultrathin graphene encapsulated Cu nanoparticles: a highly stable and efficient catalyst for photocatalytic H_2 evolution and degradation of isopropanol. Chem. Eng. J. 390, 124558.

Sarkar, C., Paul, R., Shit, S.C., Trinh, Q.T., Koley, P., Rao, B.S., Beale, A.M., Pao, C.W., Banerjee, A., and Mondal, J. (2021). Navigating copper-atom-pair structural effect inside a porous organic polymer cavity for selective hydrogenation of biomass-derived 5-hydroxymethylfurfural. ACS Sustain. Chem. Eng. 9, 2136–2151.

Stevens, M.B., Enman, L.J., Batchellor, A.S., Cosby, M.R., Vise, A.E., Trang, C.D., and Boettcher, S.W. (2017). Measurement techniques for the study of thin film heterogeneous water oxidation electrocatalysts. Chem. Mater. 29, 120–140.

Sushkevich, V.L., Safonova, O.V., Palagin, D., Newton, M.A., and van Bokhoven, J.A. (2020). Structure of copper sites in zeolites examined by Fourier and wavelet transform analysis of EXAFS. Chem. Sci. 11, 5299–5312.

Valekar, A.H., Lee, M., Yoon, J.W., Kwak, J., Hong, D.-Y., Oh, K.-R., Cha, G.-Y., Kwon, Y.-U., Jung, J., and Chang, J.-S. (2020). Catalytic transfer hydrogenation of furfural to furfuryl alcohol under mild conditions over Zr-MOFs: exploring the role of metal node coordination and modification. ACS Catal. 10, 3720–3732.

Valtchev, V. (2002). Silicalite-1 hollow spheres and bodies with a regular system of macrocavities. Chem. Mater. 14, 4371–4377.

VandeVondele, J., Krack, M., Mohamed, F., Parrinello, M., Chassaing, T., and Hutter, J. (2005). Quickstep: fast and accurate density functional calculations using a mixed Gaussian and plane waves approach. Comput. Phys. Commun. 167, 103–128.

Villaverde, M.M., Garetto, T.F., and Marchi, A.J. (2015). Liquid-phase transfer hydrogenation of furfural to furfuryl alcohol on Cu–Mg–Al catalysts. Catal. Commun. 58, 6–10.

Wang, L., Wang, L., Meng, X., and Xiao, F.S. (2019). New strategies for the preparation of sinter-resistant metal-nanoparticle-based catalysts. Adv. Mater. 31, 1901905.

Wang, C., Liu, Y., Cui, Z., Yu, X., Zhang, X., Li, Y., Zhang, Q., Chen, L., and Ma, L. (2020a). In situ synthesis of Cu nanoparticles on carbon for highly selective hydrogenation of furfural to furfuryl alcohol by using pomelo peel as the carbon source. ACS Sustain. Chem. Eng. 8, 12944–12955.

Wang, Y., Ji, X., Meng, H., Qu, L., and Wu, X. (2020b). Fabrication of high-silica Cu/ZSM-5 with confinement encapsulated Cu-based active species for NH3-SCR. Catal. Commun. 138, 105969.

Xu, J., Ji, W., Shen, Z., Tang, S., Ye, X., Jia, D., and Xin, X. (1999a). Preparation and characterization of CuO nanocrystals. J. Solid State Chem. 147, 516–519.

Xu, J., Ji, W., Shen, Z., Li, W., Tang, S., Ye, X., Jia, D., and Xin, X. (1999b). Raman spectra of CuO nanocrystals. J. Raman Spectrosc. 30, 413–415.

Yan, Y., Zhang, Z., Bak, S.-M., Yao, S., Hu, X., Shadike, Z., Do-Thanh, C.-L., Zhang, F., Chen, H., Lyu, X., et al. (2019). Confinement of ultrasmall cobalt oxide clusters within

silicalite-1 crystals for efficient conversion of fructose into methyl lactate. ACS Catal. *9*, 1923–1930.

Zabed, H., Sahu, J., Suely, A., Boyce, A., and Faruq, G. (2017). Bioethanol production from renewable sources: current perspectives and technological progress. Renew. Sustain. Energy Rev. *71*, 475–501.

Zhang, J., and Chen, J. (2017). Selective transfer hydrogenation of biomass-based furfural and 5-hydroxymethylfurfural over hydrotalcite-derived copper catalysts using methanol as a hydrogen donor. ACS Sustain. Chem. Eng. *5*, 5982–5993.

Zhang, Z., Pei, Z., Chen, H., Chen, K., Hou, Z., Lu, X., Ouyang, P., and Fu, J. (2018a). Catalytic in-situ hydrogenation of furfural over bimetallic Cu–Ni alloy catalysts in isopropanol. Ind. Eng. Chem. Res. *57*, 4225–4230.

Zhang, Z., Yang, Q., Chen, H., Chen, K., Lu, X., Ouyang, P., Fi, J., and Chen, J.G. (2018b). Efficient catalytic transfer hydrogenation of furfural to furfuryl alcohol in near-critical isopropanol over Cu/MgO-Al$_2$O$_3$ catalyst. Green. Chem. *20*, 197–205.

Zhang, Z., Jing, M., Chen, H., Okejiri, F., Liu, J., Leng, Y., Liu, H., Song, W., Hou, Z., Lu, X., et al. (2020). Transfer hydrogenation of fatty acids on Cu/ZrO$_2$: demystifying the role of carrier structure and metal–support interface. ACS Catal. *10*, 9098–9108.

STAR★METHODS

KEY RESOURCES TABLE

REAGENT or RESOURCE	SOURCE	IDENTIFIER
Chemicals, peptides, and recombinant proteins		
Silica gel (30 wt% in H_2O)	ACMEC	CAS: 112926-00-8
Furfural	Aladdin Industrial Co., China	CAS: 98-01-1
Furfuryl alcohol	Mecklin Co., China	CAS: 98-00-0
Polyvinylpyrrolidone, PVP	Mecklin Co., China	CAS: 9003-39-8
Tetrapropyl ammonium hydroxide aqueous solution (TPAOH in H_2O, 25 wt%)	Urchem, China	CAS: 4499-86-9
CuO	Sinopharm Chemical Reagent Co., China	CAS: 1317-38-0
Ethanol	Sinopharm Chemical Reagent Co., China	CAS: 64-17-5
Ammonia solution	Sinopharm Chemical Reagent Co., China	CAS: 1336-21-6
Copper nitrate trihydrate	Mecklin Co., China	CAS: 10031-43-3
5-hydroxymethylfurfural (5-HMF)	Aladdin Industrial Co., China	CAS: 67-47-0
5-methylfurfural (5-MF)	Aladdin Industrial Co., China	CAS: 210-622-6
5-methylfurfuryl alcohol (MFA)	Aladdin Industrial Co., China	CAS: 3857-25-8
2,5-furandimethanol (2,5-DHMF)	Aladdin Industrial Co., China	CAS: 1883-75-6
Software and algorithms		
CP2K	Open source	https://www.cp2k.org
Other		
PANalytical B.V. Empyrean 200895	Malvern Panalytical Ltd.	https://www.malvernpanalytical.com/en/products/product-range/empyrean-range
Tecnai G2 F20 S-TWIN and Titan ChemiSTEM G2 60-300	Thermo Fisher Scientific	https://www.fei.com/products/tem/tecnai-g2-spirit-for-life-sciences/
ESCALAB-250Xi	Thermo Fisher Scientific	https://www.thermofisher.cn/order/catalog/product/SID-10148252#/SID-10148252
METTLER TOLEDO TGA	Mettler Toledo International Co.	https://www.mt.com/cn/zh/home/products/Laboratory_Analytics_Browse/TA_Family_Browse/TGA.html
Micromeritics TriStar sorptometer	Micromeritics Instrument Co.	https://www.micromeritics.com/tristar-ii-plus/
Horiba Jobin Yvon LabRAM HR Evolution spectrometer	HORIBA, Ltd.	https://www.horiba.com/cn/scientific/products/raman-spectroscopy/raman-afm-and-nano-raman/horiba-ters-probes/
Thermo scientific Nicolet iS50 spectrometer	Thermo Fisher Scientific	https://www.thermofisher.cn/order/catalog/product/IQLAADGAAGFAHDMAZA#/IQLAADGAAGFAHDMAZA
Agilent 730 ICP-OES plasma-spec-II spectrometer	Agilent Technologies, Inc.	https://www.agilent.com.cn/zh-cn/product/atomic-spectroscopy/inductively-coupled-plasma-optical-emission-spectroscopy-icp-oes/icp-oes-instruments/5900-icp-oes
the Beijing Synchrotron Radiation Facility	the Beijing Synchrotron Radiation Facility	http://www.ihep.cas.cn/dkxzz/bsrf/

RESOURCE AVAILABILITY

Lead contact

Further information and requests for resources should be directed to and will be fulfilled by the lead contact, Jie Fu (jiefu@zju.edu.cn).

Materials availability

All materials generated in this study are available from the lead contact without restriction.

Data and code availability

All data used in the study are included in this publication and would be made available upon request. The present research did not use any new codes.

METHOD DETAILS

Catalyst synthesis

The CuO@silicalite-1 (CuO@sil-1) catalyst was synthesized via a steam-assisted crystallization method. Specifically, a known quantity of $Cu(NO_3)_2 \cdot 3H_2O$ and 0.1 g of PVP were added into 50 mL of deionized water and stirred until fully dissolved. Following this, an excess amount of ammonia solution was added and stirred for an additional 10 min. Silica gel and TPAOH with a molar ratio of 8:1 were simultaneously added to the above solution and stirred for an extra 15 min. The resultant suspension was completely dried under reduced pressure at 50°C. The dry gel was recovered and transferred into a 50 mL Teflon cup, and then placed inside a 100 mL crystallization reactor. A known volume of deionized water was introduced into the space between the Teflon cup and reactor such that the molar ratio of water to dry gel is 1:5. The reactor was sealed and then heated at 130°C for 72 hr to obtain a dark-green solid. The solid was filtered, washed three times with deionized water and ethanol, and dried thoroughly. The final catalyst was calcined at 550°C for 6 hr at a heating rate of 2°C/min. The synthesized catalysts are denoted to as 3CuO@sil-1, 7CuO/sil-1(7CuO/SiO$_2$), and 23CuO/sil-1(23CuO/SiO$_2$), where 3, 7, and 23 represent the actual Cu weight loading (Table S1), '@' and '/' represent the encapsulation structure, and conventional surface-dispersed structure respectively. The blank silicalite-1 (sil-1) was prepared by a similar method described above but without the addition of $Cu(NO_3)_2 \cdot 3H_2O$. 3CuO/sil-1 was synthesized by a post-impregnation method with a certain amount of aqueous $Cu(NO_3)_2 \cdot 3H_2O$. After impregnation, the as-obtained intermediate was dried and calcined under the same condition as 3CuO@sil-1.

Characterizations

The powder X-ray diffraction (XRD) patterns were collected on PANalytical B.V. Empyrean 200895 with Cu K$_\alpha$ radiation (λ = 1.54056 Å) at a scanning rate of 5° min^{-1} from 10° to 80°. The transmission electron microscopy (TEM) images, high-resolution TEM (HRTEM), and the high-angle annular dark-field-scanning-transmission electron microscopy (HAADF-STEM), as well as the energy-dispersive X-ray spectroscopy (EDS-mapping) spectra, were acquired on the transmission electron microscope (Tecnai G2 F20 S-TWIN and Titan ChemiSTEM G2 60-300, FEI, USA). X-ray photoelectron spectroscopy (XPS) spectra were collected on a Thermo Fisher ESCALAB-250Xi using Al Kα (1486.6 eV photons) as the radiation source. All measured peaks were calibrated by C 1s peak. The thermogravimetric analysis (TGA) curves were acquired on METTLER TOLEDO TGA 2 instrument in the air. N_2 adsorption-desorption isotherms were measured at 77 K by Micromeritics TriStar sorptometer instrument. The surface area was determined by using the Brunauer-Emmett-Teller (BET) method. The Raman spectra were acquired on the Horiba Jobin Yvon LabRAM HR Evolution spectrometer with radiation of Ar laser at 532 nm. Fourier transform infrared (FTIR) spectra were collected on Thermo scientific Nicolet iS50 spectrometer. The metal loading was determined by inductively coupled plasma optical emission spectroscopy (ICP-OES) analysis performed on an Agilent 730 ICP-OES plasma-spec-II spectrometer. The Cu K edge X-ray absorption spectra were collected at the 1W1B beamline of the Beijing Synchrotron Radiation Facility. The samples were smeared and sealed in the KaptonTM tape and collected with the fluorescence mode using a passivated implanted planar silicon (PIPS) detector. The collected spectra were treated and fitted using the Ifeffit software package. The wavelet transform provides information for both the radical distance and in *k*-space. The wavelet transform was performed based on the Morlet wavelet (Morlet et al., 1982; Grossmann and Morlet., 1984), which is obtained by taking a complex sine wave and by confining it with a Gaussian (shell-based) envelope: $\psi(k) = \frac{1}{(2\pi)^{1/2}\sigma}\exp(i\eta k)\exp(-k^2/2\sigma^2)$. To optimize the resolution for both k and R based on the $k^2\chi(k)$ EAXFS signal, η was set to 1, and σ was set 3 for all our wavelet transform analyses.

DFT calculations

The periodic density functional theory (DFT) calculations were performed using the CP2K package (Lippert et al., 1999; VandeVondele et al., 2005). The exchange-correlation potential was described using the Perdew-Burke-Ernzerh (PBE) form of the generalized gradient approximation (GGA) (Perdew et al., 1996). The

wave functions were expanded in a molecularly optimized double-Gaussian basis set, with an auxiliary plane-wave basis set with a cutoff energy of 600 Rydberg. The scalar relativistic norm-conserving pseudo-potentials were employed to model the core electrons (Goedecker et al., 1996) with 11, 6, and 4 valence electrons for Cu, O, and Si. The only Γ-point in reciprocal space mesh was used for integrating the Brillouin zone. The lattice parameters of 3CuO@sil-1, consisting of 579 atoms (192Si+381O+6Cu), are determined to be a = 26.694 Å, b = 20.082 Å, and c = 19.827 Å ($\alpha = \beta = \gamma = 90°$). The convergence criterion for the maximum force is set as $6*10^{-4}$ atomic units.

Catalytic performance evaluation

In a typical experiment, 60 mg of furfural, 30 mg of catalyst, and 6 mL of ethanol are charged into a 14 mL stainless steel batch reactor and sealed properly. The reactor is placed into a furnace preheated to the target temperature. When the reaction is completed, the reactor is removed from the furnace and immediately cooled to room temperature by running tap water. The products are collected and rinsed into a 25 mL volumetric flask using acetone and then filtered through a 0.45 μm organic filter-membrane in readiness for quantitative GC-FID analysis. For the catalyst recycling experiment, the reused catalysts are regenerated after washing severally with ethanol and drying in a vacuum oven.

QUANTIFICATION AND STATISTICAL ANALYSIS

Data was analyzed using OriginPro 2017 (OriginLab Cor., Northampton, Massachusrtts, USA). All pooled data are presented as mean $\pm$ standard error of the mean (SEM). Please see individual figure legends for details regarding number of replicates.